Evaluation of a wheel-based seismic acquisition system for a planetary rover

J. M. Lorenzo[1], A. Bates[1], D. A. Patterson[1], C. Sun[2], T. A. Douglas[3], S. Karunatillake[1], P. M. Bremner[4], M. R. Zanetti[4], H. F. Haviland[4], R. C. Weber[4], and A. J. Gemer[5]

https://doi.org/10.1190/tle41100681.1

Abstract

Prior to using in-situ planetary resources, efficient mapping of geochemical and physical characteristics of the near surface will be required. As part of an integrated geophysical instrument suite on exploration and prospecting vehicles, we investigated the suitability of seismic piezo-sensors rigidly mounted on the interior of a generic rover wheel. Factors that can compromise proper data acquisition for this system include the natural mechanical resonance of the wheel and wheel-to-ground coupling. We characterized the natural resonance frequency bands of a generic wheel with an electromagnetic shaker. We also collected seismic shot gathers for subsequent seismic surface-wave analysis using a wheel in both a dry, laboratory sand tank (1.8 × 1.8 × 0.6 m) and in frozen loess soils within the United States Army Corps of Engineers Permafrost Tunnel in Alaska. For our wheel, self-weighted coupling to the ground was found to be adequate, although suitable wheelbase dimensions can constrain field acquisition geometries. In unconsolidated sediments, represented by medium sand (0.25–0.5 mm), wheel resonance of 1 kHz does not affect the fundamental mode used in shear-wave-velocity-to-depth inversion. When analyzed, shot-gather data collected from both wheel-mounted sensors and sand-planted sensors, in loose dry sand, effectively captured similar fundamental surface-wave modes. This is evident in frequency-versus-phase velocity dispersion images. Because narrow frequency bands of wheel resonance exhibit a high signal-to-noise ratio, they also readily detect lateral attenuation changes. Thus, wheel resonance can also be used to capture soil attenuation changes, including those produced when pore H_2O ice acts to cement the regolith or loose-grained soils.

Introduction

Shallow (less than 5 m) water ice on Mars and the moon may become an essential resource for providing fuel and water in future human missions and infrastructure development. Understanding the distribution of shallowly buried ice (Cannon and Britt, 2020) may also help constrain the relative roles of precipitation, brines, and obliquity cycles (Karunatillake et al., 2021), as well as the role sublimation may play in surface terrain morphology (Douglas and Mellon, 2019). On Mars, shallow ground ice is the result of atmosphere-regolith interactions in the critical zone for habitability (Vos et al., 2019). On the moon, cold-trapped, subsurface H_2O ice in permanently shadowed regions may be key to understanding the evolution of volatiles in the solar system (e.g., Bandfield et al., 2018; NASEM, 2022). However, the roles that impact gardening, solar winds, and past volcanism play in volatile transport processes, and how these processes control variations in regolith H_2O ice, remain poorly defined on the moon (e.g., LEAG, 2016). For example, the expected distribution of H_2O ice at decimeter depths derived from thermal models differs from those estimated using neutron spectroscopy (Siegler et al., 2014).

Efficient and detailed geophysical mapping of potential ice localities, employing a grid-wise search, is required to differentiate anomalous physical property values. A suitable mobile exploration instrument, such as a rover, can provide minimal disruption to the subsurface geologic record during sampling (Figure 1). Soils of the moon and Mars are expected to be heterogeneous, varying in both composition and structure, at scales of a meter or less (Figure 1). The lunar regolith, which varies in average depth from about 7 m in the lunar maria to about 17 m in the older highlands, is poorly sorted (e.g., Slyuta, 2014; Xiao and Head, 2020).

On Earth, near-surface properties and processes can be investigated in-situ via colocated measurements of different physical properties (e.g., electromagnetic, seismic, nuclear). On Mars and the moon, examination of a very shallow target of interest (order 10^{-1} m), could combine: (1) high-frequency ground seismic, (2) ground-penetrating radar (GPR), plus (3) gamma-ray and neutron spectroscopy (e.g., 2023 VIPER mission to the moon). Compact neutron spectroscopy can detect H_2O ice down to 1 m. GPR images the dielectric contrasts in the lunar regolith (less than 40 m depth: Fa et al., 2015; Li et al., 2020) at a resolution of less than 1 m, a technique used to identify H_2O. Finally, an analysis of the seismic wavefield can help determine the geomechanical and geotechnical state of the subsurface (Brown and Rix, 1992). In contrast to invasive tools used to determine soil mechanical properties, a wheel-based seismic system collects data without disturbing the regolith.

Classically, near-surface shear waves generated by artificial sources (e.g., weight drops, electromechanical vibrators) have been used to study the rigidity of soils in the near surface; these could serve the same purpose on Mars or the moon. Modeled shear-wave velocity (V_S)-versus-depth estimates can be taken from the dispersive behavior of Rayleigh waves (Heisey et al., 1982; Stokoe

[1]Louisiana State University, Department of Geology and Geophysics, Baton Rouge, Louisiana, USA. E-mail: gllore@lsu.edu; abate15@lsu.edu; dpatterson21@cox.net; sunitiw@lsu.edu.
[2]Louisiana State University, Department of Civil and Environmental Engineering, Baton Rouge, Louisiana, USA. E-mail: csun@lsu.edu.
[3]U.S. Army Cold Regions Research and Engineering Laboratory, Fort Wainwright, Alaska, USA. E-mail: thomas.a.douglas@usace.army.mil.
[4]NASA Marshall Space Flight Center, Huntsville, Alabama, USA. E-mail: paul.m.bremner@nasa.gov; michael.r.zanetti@nasa.gov; heidi.haviland@nasa.gov; renee.c.weber@nasa.gov.
[5]Lunar Outpost Inc., Golden, Colorado, USA. E-mail: aj@lunaroutpost.com.

et al., 1994). In a heterogeneously layered medium, Rayleigh waves display a characteristically identifiable dependency between phase velocity and frequency, known as dispersion. When the fundamental-mode phase velocities are calculated accurately, reliable S-wave velocities can be also estimated within ± 15% accuracy of borehole measurements (Xia et al., 2002).

Rayleigh wave modes are easily detected because they generally have a higher natural signal-to-noise ratio (S/N) than body waves. Surface-wave amplitudes only decay at $1/r$ in comparison to refracted body waves ($1/r^2$) where r is the total distance of travel between source and receiver (e.g., Park, 2013). They also have the distinct advantage of detecting low-velocity zones (De Nil, 2005). Although seismic reflection images have proven especially sensitive to the presence of pore-saturated, interstitial frozen ice (Johansen et al., 2003) in "deep" settings (more than 10 m), they are logistically complex to collect because they require a large number of sensors (approximately 10^1: e.g., Yilmaz, 2001) to compensate for usually weak reflected signals.

We can use conservative estimations of the general seismic behavior in order to match wheel design to exploration depths using Rayleigh waves (Figure 2). A nominal depth of investigation will range between one-half and one-third of the dominant wavelength of the fundamental mode (Foti et al., 2014). If we assume a P-wave to S-wave velocity ratio (V_P/V_S) of 2 and a bandwidth of 0.1 to 1 kHz the nominal depth will be 10^{-2} to 10^1 m. We use recently modeled seismic data from Mars (P-wave velocity [V_P] = approximately 100 to 400 m/s: Lognonné et al., 2020) and shallow velocity-to-depth models from Apollo active experiments (V_P = 100 to 114 m/s: Cooper et al., 1974; Sollberger et al., 2016; Heffels et al., 2017; Figure 3). Data collection is best when limited to moments when the rover is stopped so as to reduce unwanted noise from interactions between the wheel and underlying soil.

For surface waves, the intrinsic seismic attenuation of soils will also independently affect the depths to which signals can travel and maintain an amplitude above the background noise level. Seismic attenuation is often presented in terms of energy stored versus energy lost per wavelength during travel, by the seismic quality factor (Q; Knopoff, 1964), where attenuation = Q^{-1}. That is, for equal travel distances, shorter wavelength components of the wavefield experience greater intrinsic attenuation than longer wavelengths. Although longer wavelengths can sample to greater depths, they have poorer resolution. For any given

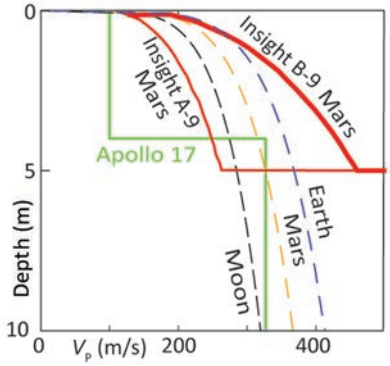

Figure 2. Estimates of V_P versus depth in regolith, created using either contact theory (CT-dashed lines) or data (continuous lines), collected on the moon and Mars. In CT, the major differences are caused by differences in gravity. CT cases assume approximately 50% porosity and 0.25 mm grain diameter. Earth and moon cases use a quartz mineralogy and Mars, a JSC-1 simulant (Allen et al., 1998). Mars Insight data-derived models come from Lognonné et al. (2020). Apollo 17 case comes from Cooper et al. (1974).

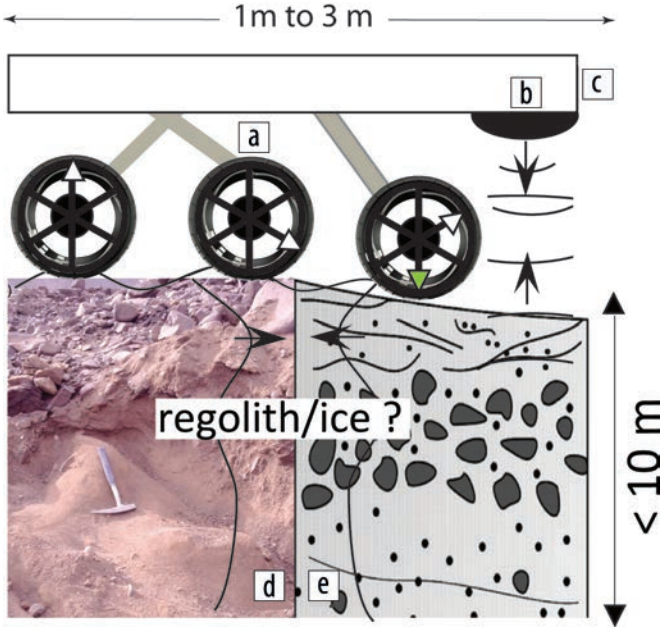

Figure 1. (a) Piezo-ceramic sensors (white triangles) and source (green triangles) receive and transmit surface waves through the wheel structure coupled to soil (not to scale). (b) GPR transceiver detects electromagnetic properties, and (c) a gamma-ray-neutron-spectrometer sensor collects background compositional energies. (d) Antarctic Dry Valley Mars analogue (Heldmann et al., 2013) and (e) shallow GPR results from the moon (Fa et al., 2015) predict a heterogeneous soil-H_2O ice mixture that requires an integrated suite of geophysical tools to detect.

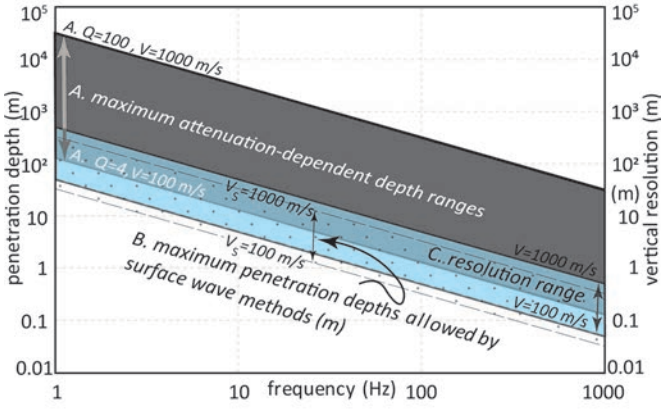

Figure 3. Conservative estimates of penetration/target depths (m) imposed by natural seismic attenuation and surface-wave methods (left vertical axis). Vertical seismic resolution estimates plot on the right vertical axis. V without subscript refers to either V_P or V_S. Estimates range for cases between 100 and 1000 m/s. Both axes plot using $\log_{10}$ scales. Quality factor Q = 1/intrinsic attenuation. (a) Maximum penetration depths allowed by attenuation for "soft" (Q = 4) and "hard" (Q = 100) materials are indicated by a gray-colored background, bracketed by a continuous black or gray line. Depths are calculated for when amplitude decays to 1/e of the original value. (b) Maximum penetration depths allowed by surface-wave methods assume a wavelength/3 criterion and are indicated by a stippled area bracketed by dashed gray lines. (c) Vertical resolution assumes a wavelength/2 criterion and is also marked using a blue background.

DOI:10.1190/leedff.2022.41.issue-10

frequency, if seismic attenuation is too high (Q less than 10; Figure 3), as in dry, unconsolidated sand (Q = 4 to 6 for P-waves: Crane et al., 2018), some target depths are unattainable. Intrinsic seismic attenuation may result from friction between the grains due to sorting, roundness, and compaction.

Experimental results show that both Q (Figure 4) and measured V_P and V_S increase concomitantly with the degree of pore ice saturation (Park and Lee, 2014), under the assumption that ice acts to increase the overall rigidity of the material by cementation across the pore spaces. Attenuation is expected to be several orders of magnitude less on the moon than on Earth (Blanchette-Guertin et al., 2012), implying seismic penetration depth on the moon may not be as limited.

Wheel-based seismic sensors represent a previously unused and novel technique for seismic acquisition on a rover. Here, we address some key design elements that influence the potential feasibility and performance of a high-frequency (less than 1 kHz) seismic system for planetary rover wheels. We conduct exploratory resonance tests on a generic aluminum wheel and compare recorded data quality between piezo-sensors planted directly in loose sand and those mounted rigidly to the wheel. We do not discount that surface-wave studies can capture independent complementary refracted P-wave arrivals, but rather we emphasize the value of dominant surface-wave components.

Background

Rock-physics models for the moon and Mars. The suitability of high-frequency sensors can also be addressed by considering heuristic rock-physics models (Figure 1) and experimental results (Figure 4) from laboratory and/or field analogues. General contact theory models (Mindlin, 1949; Mavko et al., 2009) for granular media consider that gravity, bulk density, rigidity, porosity, and contact number are key properties. There is considerable overlap in the value of these properties across different silicate minerals. For initial simplicity, in the laboratory we use quartz sand (Table 1) to estimate the quality of wheel-soil coupling and accompanying wheel resonance behavior. For lunar regolith, at least five compositionally distinct igneous rock types are recognized (e.g., Xiao and Head, 2020). Mars regolith simulants (e.g., JPL-107 and MER-317; Perko et al., 2006) also capture a range of mineralogies (quartz to basaltic volcanic ash). If ice is considered to bond soil grains together, then cemented contact theory, in combination with effective medium theory (Dvorkin et al., 1999), can be used

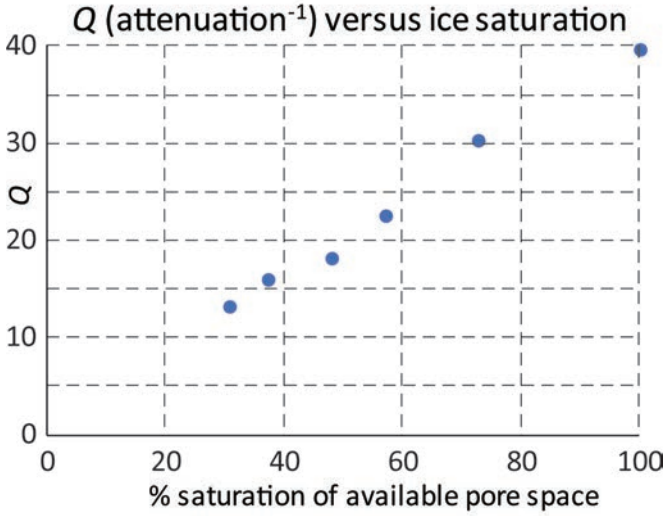

Figure 4. Based on experimental results (Nakano and Arnold, 1973), if pore H_2O ice acts to cement granular materials, the seismic attenuation is expected to decrease with greater abundance of ice.

Table 1. Source and sensor equipment and software, and seismic acquisition parameters, for laboratory and field tests. The limiting noise level of the complete sensor-recording systems is 1 to 10 mV.

Seismic sensors and acquisition system	
Sensor characteristics	Sand tank: Piezo-electric accelerometer of polyvinylidene fluoride film composition (ACH-01; from Measurement Specialties Inc.); nominally flat response of about 9 mV/g ± 1 mV/g between 20 Hz and 20 kHz; noise floor at 1 kHz: 6 mg/Hz$^{0.5}$, 8 grams mass. Alaska field test: Piezo-ceramic PCB M356A7, 3-axes, 10 pC/g, (12 × 24 × 9) mm, 23 grams mass.
Source wavelets	Sand tank: in-house pulser with 140 V peak-to-peak, 10 µs rise and fall times, 1 mJ per pulse.
Sensor spacing	Sand tank: 5 cm. Alaska field tests: 10 cm.
Wheel	6061 Aluminum, 25 cm diameter × 19 cm width, 2.25 kg.
Signal conditioning	Sand tank: Voltage-based in-house × 1 operational amplifier with +12 V, –12 V DC power source, VRMS noise 1 to 10 mV; 5-to-40 summed data stacks per location. Alaska field test: in-house, low-noise, current-based amplifier.
	Recording electronics (10 mV_{RMS} noise level)
Nyquist frequency	Sand tank: 3.9 kHz on 16-bit, National Instruments PC6251 acquisition card. Alaska field test: 4 kHz on 24-bit, commercial field seismic unit.
Seismic source/actuator	Sand tank: Piezo-ceramic NEC-Tokin multilayer actuator, (7 × 7 × 10) mm, approximately 9 micro-m displacement, capped by (8 × 8 × 2) mm plastic plate all loaded with 5 cm diameter × 7 cm tall, 1.6 kg lead weight (Figure 7c). Alaska field test: 0.75 kg drop-weight from 10 cm (0.735 J per blow).
Seismic software	Seismic Unix Processing System (Stockwell, 1999); filtering, manipulation, and display.
Sand tank	Interior (1.8 × 1.8 × 0.6) m, 7 cm layer of angular, medium sand, mean diameter = 0.29 mm, underlain by 4 cm of rounded quartz gravel and cobbles.

to predict V_P and V_S for the full range of ice saturation in the pore spaces (Johansen et al., 2013).

Seismic field and laboratory methods. Weight, power requirements, and durability under extreme temperatures and radiation, are some factors constraining deployment of seismic instrumentation on planetary bodies. Synthetic piezo-actuators made of ceramic lead zirconate titanate materials have long been under consideration by NASA (Hooker, 1998; Xu et al., 2015) because of their small size (cm^3), endurance, and performance in aerospace applications. Piezo-electric ceramics (PZT-5A) were chosen for the Huygens lander on Titan because of their durable performance, despite exposure to prolonged low space temperatures and radiation levels over the seven-year mission. Additionally, piezo-ceramics can also act as seismic source generator/actuators (Table 1). Lead magnesium niobate (PMN) and PMN-PT (titanate) are examples of well-known electrostrictive materials (e.g., Blackwood and Ealey, 1993) currently commercially available for use, especially in cryogenic (NIST below –180°C) space-like conditions. Piezo-ceramics can also maintain their performance characteristics after exposure to the equivalent of 10 years of high radiation in Earth orbit (20 krad: Lorenz et al., 1994). Additionally, piezo-electric materials can act both as sensors and sources; they will produce an electric charge when stressed and conversely change shape when subjected to an electrical potential difference.

For the laboratory sand tank (Table 1), we use a low-weight (4 g) piezo-ceramic source and piezo-polymer (polyvinylidene fluoride [PVDF]) sensors that are well established (Lorenzo et al., 2013) and low-cost equivalents to piezo-ceramic materials. As is standard in near-surface seismology acquisition, we improve the source-ground coupling by placing a small plate (Table 1; Figure 7c) between the source and the underlying sand. The plate is slightly larger in length and width (Table 1) than the head of the piezo-source. We interpret that the plate acts to reduce the pressure on the sand so more energy is transferred as elastic strain rather than permanent shear deformation among the grains of sand. A weight (Table 1) placed on top of the piezo-source ensures most of the source acceleration is directed downward.

Nevertheless, we find that after repeated impacts (more than five times) we have to reseat the piezo-source to maintain good signal strength, possibly because the source vibration eventually moves the sand particles away from the effective range of the expanding and contracting piezo-source. Although they are an order of magnitude more sensitive than piezo-ceramic and natural crystals, PVDF sensors lose sensitivity under colder conditions where piezo-ceramic materials perform better. Inside the Permafrost Tunnel we switched to a single, three-component piezo-ceramic accelerometer rigidly mounted to the interior of the aluminum wheel, and a small weight drop (Table 1). We use both 16-bit and 24-bit digital acquisition systems (Table 1) in the sand tank and in the field, respectively.

Like many other investigators, we apply a standard 2D spectral decomposition (seismic phase velocity versus frequency) on the vertical component of the seismic data to generate surface-wave dispersion images (e.g., Park et al., 1999; Xia et al., 1999). We interpret the trend of the fundamental mode to derive a 1D V_S-depth model (Wathelet, 2008) in the sand tank. However, seismic records may be contaminated with reflected, refracted, and backscattered waves and local environmental noise. For example, backscattered surface waves can generate negative apparent velocities. We also consider that reflections from the walls of the small sand tank we employ may create false high phase velocities if the returning wavefront is almost parallel to the linear sensor array. We attempt to minimize these effects by excluding dispersion calculations with negative phase velocity values and interpreting surface-wave modes using the smallest reasonable phase velocity value at each frequency. Our initial model for the inversion comprises nine homogeneous layers, each potentially 0.1 to 1 cm thick, and equally broad constraints for V_S (5 to 400 m/s), V_P (10 to 400m/s), density (1600 to 2000 kg/m^3), and Poisson's ratio (0.2–0.5).

We conducted initial field tests at the U.S. Army Corps of Engineers Cold Regions Research and Engineering Laboratory's Permafrost Tunnel Research Facility near Fairbanks, Alaska, considering it to be a convenient terrestrial analogue to cryospheric processes on Mars (Douglas and Mellon, 2019). This unique underground research facility (Douglas et al., 2011) is 500 m long and traverses intact, syngenetic, ice-rich permafrost. This site offers the potential to evaluate the effects of pore ice on seismic attenuation in otherwise loose granular materials for both the moon and Mars cases. Seismic velocity information was not collected, but V_S values from previous surface-wave studies (Cox et al., 2012) show that shear-wave velocities in frozen ground (Figure 5) generally exceed 400 m/s.

We evaluate the influence of the wheel's natural frequency on the performance of wheel-mounted accelerometers, numerically (Figure 6) and physically (Figure 7). We create a finite element model (using ANSYS software) of an equivalent wheel to gain a

Figure 5. Field deployment of wheel-mounted three-component accelerometer in permafrost loess cave, Alaska. Hammer drop (Table 1) is the source.

general but initial understanding of the wheel resonance behavior. Subsequently we use an electromagnetic shaker to oscillate the rigidly attached wheel over a broad frequency range of 10 Hz to 10 kHz. Amplitudes are made to vary sinusoidally, and all motion is kept vertical. We place six sets of three, single-component accelerometers, spaced every 60° around the rim interior of a generic rover wheel (Figure 7).

Various methods to determine surface-wave attenuation can be applied to surface-wave data sets similar to ours (Kudo and Shima, 1970). We evaluate whether variations in estimated attenuation can be used as a proxy for changes between soils possibly hardened by ice cementation and "soft" regolith. A simple, low-cost, and efficient comparison of attenuation between different data sets involves a linear regression of the measured acceleration as a function of distance between source and sensor (Foti et al., 2014).

Results

A preliminary vibrational analysis of a simple wheel over a nominally useful range of less than 1 kHz predicts 10 modes of complex vibrations (Figure 6). In response to vertical motion, we find that radial and circumferential deformation dominates the first mode, and axial deformation dominates the second mode. More complex vibration modes can be observed in higher-order modes of the wheel, including out-of-plane bending. However, radial deformations dominate the predicted multiple resonant frequencies and deformation modes. Complementary testing on an electromagnetic shaker confirms the general first-order numerical results. Bode plot displays (Figure 8) show that for vertical shaker motion, in the range less than 1 kHz, the amplitude of the radial wheel resonance response exceeds other components by an average of 25 dB.

In the case of laboratory sand-tank experiments, the natural wheel resonance near 1 kHz (Figure 8) does not interrupt fundamental or higher-order modes (Figure 9a) captured in the dispersion images (Figures 9d and 9e). The spectral amplitude plot for the wheel-based case in the sand tank (Figure 9f) confirms the existence of high values in the resonance band out to large offsets of 1.8 m. However, their associated phase velocities exceed the range of natural values captured by the dispersion calculations. Even higher-order modes of the dispersion image (Figure 9a) lack energy near the 1 kHz level. Fundamental modes share a similar trajectory in both the wheel-mounted and sand-buried sensor cases and most likely represent the true velocity structure in the sand. The lowest frequency values of the fundamental mode (approximately 40 Hz) limit the depth of the inversion results to less than 9 cm (Figure 9c). The gradient

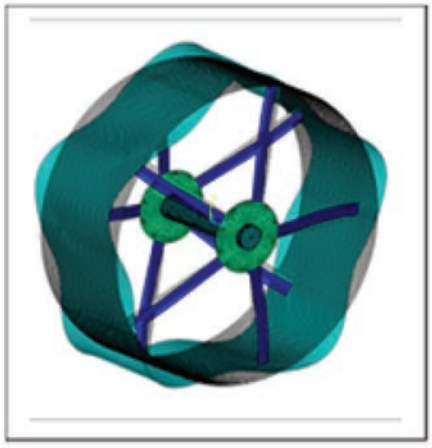

Figure 6. Meshed wheel finite element model: diameter = 250 mm; width = 100 mm. Thickness of the grouser = 2.5 mm; diameter of the central shaft = 5 mm. The grousers are modeled using titanium (Young's modulus = 105 GPa, density = 4500 kg/m^3, Poisson's ratio = 0.31). Other parts of the wheel are modeled using aluminum (Young's modulus = 69 GPa, density = 2700 kg/m^3, Poisson's ratio = 0.33). The spoke has a cross-section = 10 × 10 mm^2. Simply supported boundary conditions are applied at the two ends of the central shaft with no external loading. Eigen analysis is performed to determine the natural frequencies and mode shapes of the wheel. At the 11th mode, shapes describe a twisted deformation of the cylindrical shell.

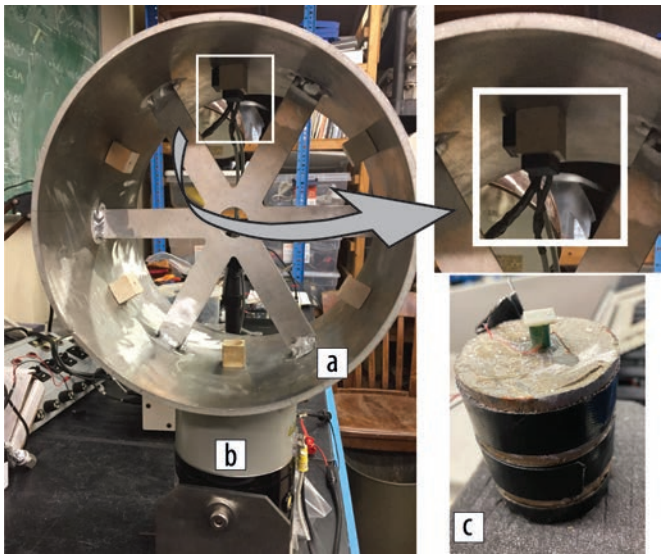

Figure 7. (a) Resonance evaluations on an aluminum wheel (25.4 dia. × 19 cm) use a (b) vertical-motion electromagnetic shaker. Inset: A wooden cube is mounted with three rigidly attached piezo-polymer accelerometers aligned into the radial, axial, and tangential directions with respect to the rotational axis of the wheel. (c) The seismic source in the sand tank comprises a lead weight, a piezo-ceramic source, and a white plastic plate (Table 1) rigidly glued together. The plate improves mechanical coupling in sand.

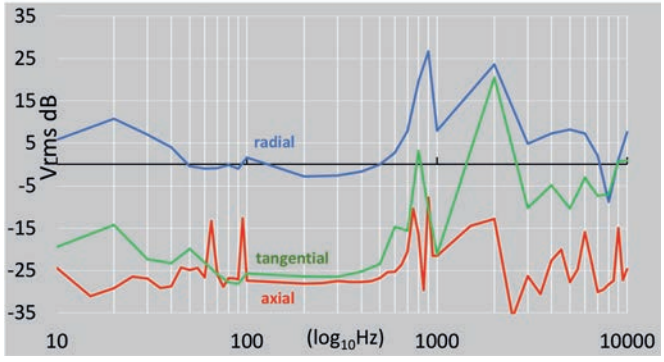

Figure 8. A representative, three-component spectral response of wheel-mounted piezo-accelerometers during a shaker test with only vertical motion. Vertical axis units are volts, V_{RMS}, and the horizontal, $\log_{10}$ axis displays shaking frequency. As expected, the strongest response occurs in the vertical direction (radial). The strongest natural resonance in the shaker-wheel-sensor system centers at 1 kHz. The most useful seismic bandwidth exists for less than 1 kHz. Resonance at 20 Hz originates from the electromagnetic shaker.

DOI:10.1190/leedff.2022.41.issue-10

in V_S values changes from 20 to 80 m/s at 6 cm depth and remains constant below this.

We can take advantage of the dominant natural resonance of the wheel, which guarantees high S/N in about the 900 Hz to 1 kHz range (Figure 9f), to measure attenuation and gain insight into the role of ice cementation on the rigidity (and lower attenuation) of permafrost. A comparison of amplitude spectra, between data collected by wheel-based sensors used in the laboratory sand-tank and wheel-based sensors used in the Alaska permafrost (Table 1), shows marked differences (Figure 10). Despite scatter in measurements of the spectral power, spectral decay occurs over much shorter distances (approximately 1 m) in the case of loose sand than in frozen soil.

Of primary importance to the suitability of surface-wave methods is that at distances less than one-half wavelength (Stokoe et al., 1994; Foti et al., 2014), surface waves may not be stabilized enough to meet the planar wave assumption, which is required for dispersion calculations. The maximum distance between sensors and sources is controlled by the rover wheelbase. For example, a source-to-receiver distance of 1 m implies that suitable wavelengths are less than 2 m. Ideally, we can meet this criterion in the case of low-velocity soils, e.g., V_S = 60 m/s on Mars (Spohn et al., 2021), if we can gather dispersion modes with frequencies in the hundreds of hertz. When V_S velocities increase, the wavelength of Rayleigh waves can exceed our maximum criterion at low frequencies; e.g.,

Discussion

For a rover, wheel design helps control the geometric distribution of seismic sensors, which in turn can predetermine the potential range of exploration depths and estimates of V_S versus depth. Optimal design factors common to all surface seismic array methods include sensor quantity, spacing, and array length (Foti et al., 2014). To collect usable surface-wave data, we can consider that current rovers may have 1 to 3 m separation between distant wheels. This means that the length of the wheelbase sets the largest Nyquist wavenumber per shot and minimum unaliased wavelength. Based on a half-wavelength criterion, the shallowest sensing depth would range from 0.5 to 1.5 m. Lateral resolution of the V_S-versus-depth models can be further improved via cross-correlation of data from sensors along a transect (Hayashi and Suzuki, 2004). Because phase-velocity estimates normally use arrays of tens of sensors per shot, rovers with only four wheels may yield inaccurate dispersion plots and V_S-depth inversions. Although each wheel containing a piezo-source can independently generate surface waves from different positions, for each shot array there are at most three wheels on the rover to record data. For this case, the surface-wave group velocity will produce a more accurate V_S-depth model (Long and Kocaoglu, 2001) than phase-velocity analyses. Group velocity can be determined by single-trace data (Luo et al., 2011), especially if the surface-wave fundamental-mode energy is dominant, thereby making even a limited rover seismic subsystem with few sensors potentially feasible.

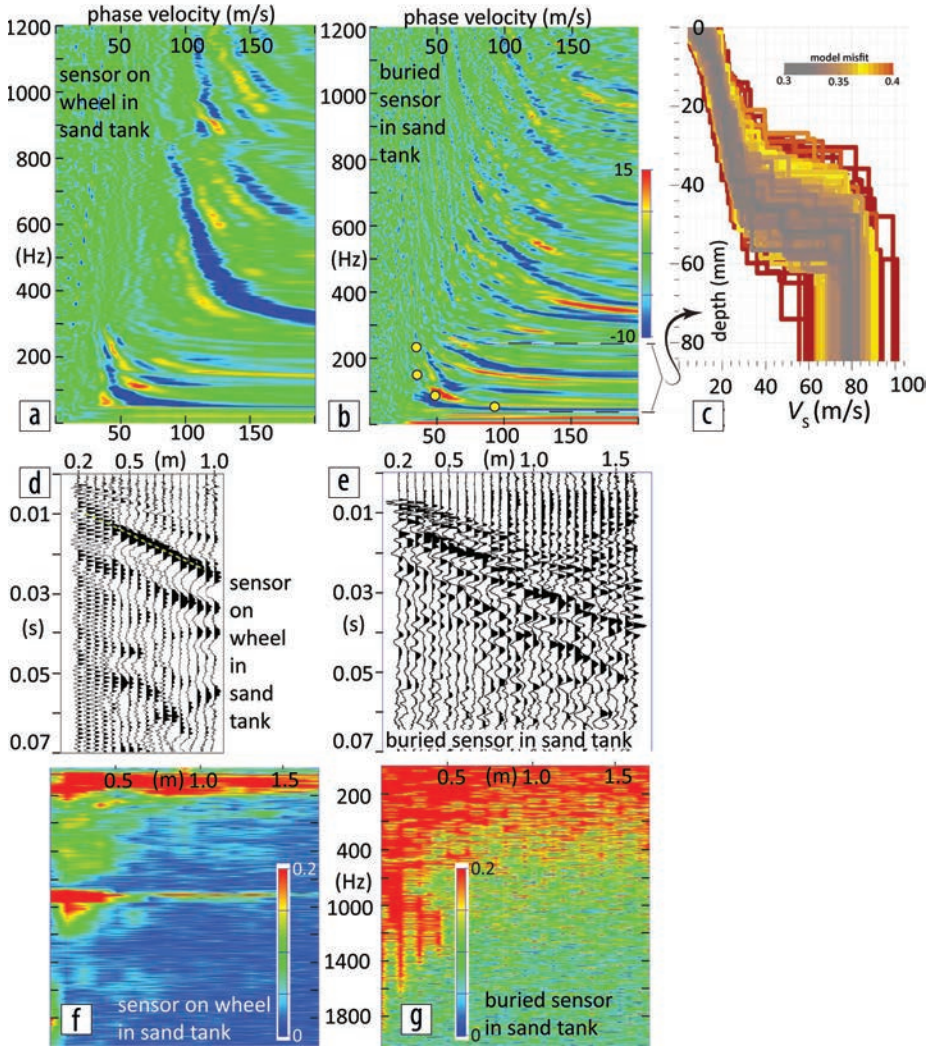

Figure 9. (a) Real component of seismic dispersion image (phase velocity versus frequency) for a single, seismic, shotpoint gather collected using a vertically oriented accelerometer (Table 1) mounted to the inside of a wheel at its apex. (b) Real component of dispersion image corresponding to data collected using vertical accelerometers buried in the sand tank. Yellow circles are the values interpreted to represent the fundamental-mode dispersion trend. (c) Resultant inversion (V_S versus depth) of the fundamental mode; the minimum misfit for 20,000 models run is 31%. Inversion of selected fundamental mode yields similar velocity depth models for both (a) and (b) cases. (d) Distance-time-amplitude plot of seismic data collected with a vertically oriented accelerometer (Table 1) mounted to the inside of a wheel at its apex. Dotted line marks possible surface wave. (e) Distance-time-amplitude plot of seismic data collected with a vertically oriented accelerometer (Table 1) buried in sand tank. (f) Amplitude spectra for case of wheel-mounted sensor. The natural resonance frequency band near 1 kHz of the wheel remains visible at the farthest offset (1.8 m). (g) Spectral amplitude plot of data collected with buried sensors in sand tank shows a general decay of amplitude with offset between the sensor and the source.

DOI:10.1190/leedff.2022.41.issue-10

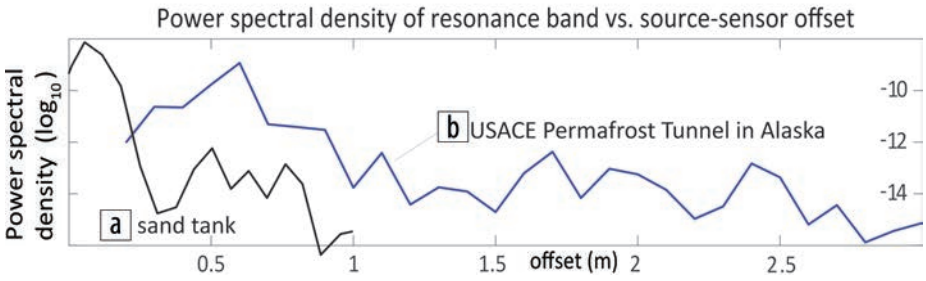

Figure 10. Power-spectral density (Welch's Method) of a 1 kHz resonant wheel frequency versus source-to-sensor offset. Both curves have been compensated for cylindrical divergence, assuming the original data represent the vertical component of planar surface waves. Power decay is greater in the (a) loose sand of the laboratory sand tank (–6 dB/m) than for the (b) Alaska permafrost field case (long blue line) where power decay with offset is –2 dB/m.

at more than 100 m/s but less than 20 Hz. Supplementary methods may include seismogram modeling of near-field body wave seismograms. Although logistically more complex, a second rover carrying a seismic source could be used to increase source-to-sensor distances. Or, as in the case of high-velocity soils of the Permafrost Tunnel (V_S = 400 m/s), a short-wheelbase rover (1 to 3 m) instead could use changing attenuation characteristics to detect changes in soil stiffness as a proxy for ice content in otherwise loose soil or regolith.

Although our results are the first of their kind and only preliminary, surface-wave analyses show favorable similarities between the cases of wheel-mounted and sand-planted sensors. We infer at present that the weight of the wheel (2.25 kg, Table 1) and small area of contact (est. 190 cm^2) confers sufficient pressure to accurately couple the wheel-mounted sensor with ground movement. On Mars and the moon, additional mass per wheel would be required to maintain a similar pressure under the lower gravity — 4.5 kg and 13.9 kg, respectively. The rover chassis and payload could provide the extra mass. However, because the piezo-source is small, we can achieve good ground coupling with an overburden mass less than that of the wheel (Table 1) and an intermediate plastic plate (Table 1) similar to commonly used aluminum plates for Earth-based surface-wave studies.

Despite H_2O-poorer conditions on Mars and especially the moon compared to Earth, plus notable differences in composition and geologic history, shallow regolith seismic velocities may be predicted (Figure 2) using contact theory and relatively simple materials like sand. Typically, highly-brecciated, shallow lunar regolith displays a P-wave velocity (V_P) of 102 m/s (Cooper et al., 1974). As such, it may be possible to predict potential target depths and seismic resolution limited by seismic attenuation (Figure 3). Seismic attenuation is important for lunar regolith or Mars soils because, for a given frequency, it reduces the seismically accessible target depths (Figure 3). In-situ H_2O ice, if present, will improve attenuation, because attenuation factors decrease by two orders of magnitude (Singhroha et al., 2016) upon entering frozen gas hydrates, an analogous frozen volatile. Both analytical (Chang and Hicher, 2009) and numerical (Jiang et al., 2013) models predict that high surface-energy forces, such as van der Waals forces, play an important role in increasing shear strength (approximately 10%). The large surface roughness of regolith particles is also often used to explain the high shear strength (Carrier et al., 1991). Friction between grains (Johnston and Toksoz, 1979) binds particles, possibly leading to less attenuation, and can contribute to greater effective elasticity. In contrast, in equivalent, dry, terrestrial silt- to sand-sized soils, in contact theory models (Mavko et al., 2009) gravitational forces dominate surface-energy forces.

Spectral dispersion images in our two cases appear insensitive to wheel resonance. Natural wheel resonance as measured with a mechanical shaker (Figures 7 and 8), if problematic, could be reduced and deconvolved from the seismic data in order to extract signal with less noise. A simpler method is to reduce the wheel size, to shift natural resonance to higher values. However, as long as sensor-to-ground coupling via the wheel remains acceptable, we find that changes in the strong S/N levels within the resonance band may be a simple means to detect changes in ground rigidity (Figure 10), such as grains cemented by H_2O ice.

Interpretation of seismic velocities in soils that contain pore ice may also be conditioned by analogy to the well-known effect of patch-size heterogeneities seen in rocks on Earth (Knight et al., 1998). We can expect the size of frozen soil patches to influence measured seismic velocity in granular soils (Shen and Lorenzo, 2016). For those cases of less than 100% ice filling the pore spaces, heterogeneity in the pore-ice patch size (or empty pore spaces) relative to the dominant wavelengths will result in different seismic velocities, even when the average ice content remains constant. In the case of Mars, ice patchiness in frozen soil may be caused by the cumulative history of sublimation and partial melting. These effects are unknown but have been speculated for brines (Rivera-Valentin et al., 2020).

Conclusions

Exploration for readily accessible H_2O ice in the shallow soil of the moon or Mars is analogous to that for any buried resource on Earth. As in the hydrocarbon industry, an integrated multitool methodology is usually the most advantageous. Although logging and coring allows direct testing and calibration of geophysical properties, in-situ drilling is a costly method and usually reserved for the final stages of exploration. Measurements at single locations cannot be readily scaled to the whole area of interest without geophysical transects to link data between wells.

Seismic surface-wave data can be collected in a small sand tank, using small-footprint, low-energy piezo-electric sensors and source/actuators rigidly mounted to a generic wheel. Dispersion images derived from the data are suitable for interpretation and inversion as V_S-depth models. Although centered at a high frequency (1 kHz), the strong S/N of the resonance may be useful in detecting buried rigid materials. Indication of the rigidly frozen loess from seismic attenuation (inverse of Q-quality factor) allows measurement of the inelastic nature of the subsurface. Ice-cemented frozen loess displays relatively lower attenuation.

A combined geophysical approach can be strategically advantageous for obtaining information on the depth and nature of

H_2O ice deposits in heterogeneous soils. Quantitatively integrated data sets provide better constrained results (Inazaki and Hayashi, 2011), and dense data sets can be handled by many geostatistical methods (e.g., Dubrule, 2003). More recently, machine learning methods are facilitating geophysical inversion (Russell, 2019) and automating resource mapping (Caté et al., 2017). TLE

Acknowledgments

We thank M. Panning, Y. Li, and two anonymous reviewers for the many insightful suggestions that helped improve this manuscript. This work was possible thanks to support from NASA EPSCoR Cooperative agreement 80NSSC20M0150 (CFDA #43.008) and Ernest and Alice Neal Professorship in Geology and Geophysics (J. M. L.). T. A. D. acknowledges the U.S. Army Futures Command and the Assistant Secretary of the Army for Acquisition, Logistics, and Technology Basic and Applied Research programs for their support.

Data and materials availability

Data associated with this research are available and can be accessed via the following URL: https://github.com/gllore/TheLeadingEdgeData.

Corresponding author: gllore@lsu.edu

References

Allen, C. C., R. V. Morris, K. M. Jager, D. V. Glen, D. J. Lindstrom, M. M. Lindstrom, and J. P. Lockwood, 1998, Martian regolith simulant JSC Mars-1: Presented at 29th Annual Lunar and Planetary Science Conference, abstract no. 1690.

Bandfield, J. L., M. J. Poston, R. L. Klima, and C. S. Edwards, 2018, Widespread distribution of OH/H_2O on the lunar surface inferred from spectral data: Nature Geoscience, **11**, 173–177, https://doi.org/10.1038/s41561-018-0065-0.

Blackwood, G. H., and M. A. Ealey, 1993, Electrostrictive behavior in lead magnesium niobate (PMN) actuators. I. Materials perspective: Smart materials and structures, **2**, no. 2, 124–133, https://doi.org/10.1088/0964-1726/2/2/008.

Blanchette-Guertin, J.-F., C. L. Johnson, and J. F. Lawrence, 2012, Investigation of scattering in lunar seismic coda: Journal of Geophysical Research: Planets, **117,** E06003, https://doi.org/10.1029/2011JE004042.

Brown, D. A., and G. Rix, 1992, Geotechnical investigation strategies for lunar base: Journal of Aerospace Engineering, **5**, no. 2, 199–213, https://doi.org/10.1061/(ASCE)0893-1321(1992)5:2(199).

Cannon, K. M., and D. T. Britt, 2020, A geologic model for lunar ice deposits at mining scales: Icarus, **347**, 113778, https://doi.org/10.1016/j.icarus.2020.113778.

Carrier III, W. D., G. R. Olhoeft, and W. Mendell, 1991, Physical properties of the lunar surface, *in* G. H. Heiken, D. T. Vaniman, and B. M. French, eds., Lunar sourcebook, a user's guide to the moon: Cambridge University Press, 475–595.

Caté, A., L. Perozzi, E. Gloaguen, and M. Blouin, 2017, Machine learning as a tool for geologists: The Leading Edge, **36**, no. 3, 215–219, https://doi.org/10.1190/tle36030215.1.

Chang, C. S., and P.-Y. Hicher, 2009, Model for granular materials with surface energy forces: Journal of Aerospace Engineering, **22**, no. 1, 43–52, https://doi.org/10.1061/(ASCE)0893-1321(2009)22:1(43).

Cooper, M. R., R. L. Kovach, and J. S. Watkins, 1974, Lunar near-surface structure: Reviews of Geophysics, **12**, no. 3, 291–308, https://doi.org/10.1029/RG012i003p00291.

Cox, B. R., C. M. Wood, and K. Hazirbaba, 2012, Frozen and unfrozen shear wave velocity seismic site classification of Fairbanks, Alaska: Journal of Cold Regions Engineering, **26**, no. 3, 118–145, https://doi.org/10.1061/(ASCE)CR.1943-5495.0000041.

Crane, J., J. M. Lorenzo, J. Shen, and C. D. White, 2018, The competing effects of stress and water saturation on in-situ Q for shallow (< 1 m), unconsolidated sand, evaluated with a modified spectral ratio method: Near Surface Geophysics, **16**, no. 2, 104–117, https://doi.org/10.3997/1873-0604.2017048.

De Nil, D., 2005, Characteristics of surface waves in media with significant vertical variations in elasto-dynamic properties: Journal of Environmental and Engineering Geophysics, **10**, no. 3, 263–274. https://doi.org/10.2113/jeeg10.3.263.

Douglas, T. A., D. Fortier, Y. L. Shur, M. Z. Kanevskiy, L. Guo, Y. Cai, and M. T. Bray, 2011, Biogeochemical and geocryological characteristics of wedge and thermokarst-cave ice in the CRREL permafrost tunnel, Alaska: Permafrost and Periglacial Processes, **22**, no. 2, 120–128, https://doi.org/10.1002/ppp.709.

Douglas, T. A., and M. T. Mellon, 2019, Sublimation of terrestrial permafrost and the implications for ice-loss processes on Mars: Nature Communications, **10**, 1716, https://doi.org/10.1038/s41467-019-09410-8.

Dubrule, O., 2003, Geostatistics for seismic data integration in Earth models: SEG, Distinguished Instructor Short Course no. 6, https://doi.org/10.1190/1.9781560801962.

Dvorkin, J., J. Berryman, and A. Nur, 1999, Elastic moduli of cemented sphere packs: Mechanics of Materials, **31**, no. 7, 461–469, https://doi.org/10.1016/S0167-6636(99)00009-5.

Fa, W., M.-H. Zhu, T. Liu, and J. B. Plescia, 2015, Regolith stratigraphy at the Chang'E-3 landing site as seen by lunar penetrating radar: Geophysical Research Letters, **42**, no. 23, 10,179–110,187, https://doi.org/https://doi.org/10.1002/2015GL066537.

Foti, S., C. G. Lai, G. J. Rix, and C. Strobbia, 2014, Surface wave methods for near-surface site characterization: CRC Press, https://doi.org/10.1201/b17268.

Hayashi, K., and H. Suzuki, 2004, CMP cross-correlation analysis of multi-channel surface-wave data: Exploration Geophysics, **35**, no. 1, 7–13, https://doi.org/10.1071/EG04007.

Heffels, A., M. Knapmeyer, J. Oberst, and I. Haase, 2017, Re-evaluation of Apollo 17 Lunar Seismic Profiling Experiment data: Planetary and Space Science, **135**, 43–54, https://doi.org/10.1016/j.pss.2016.11.007.

Heisey, J. S., K. H. Stokoe, and A. H. Meyer, 1982, Moduli of pavement systems from spectral analysis of surface waves: Transportation Research Record, **852**, 22–31.

Heldmann, J. L., W. Pollard, C. P. McKay, M. M. Marinova, A. Davila, K. E. Williams, D. Lacelle, and D. T. Andersen, 2013, The high elevation Dry Valleys in Antarctica as analog sites for subsurface ice on Mars: Planetary and Space Science, **85**, 53–58, https://doi.org/10.1016/j.pss.2013.05.019.

Hooker, M. W., 1998, Properties of PZT-based piezoelectric ceramics between –150 and 250°C: NASA Langley Research Center, NASA/CR-1998-208708.

Inazaki, T., and K. Hayashi, 2011, Utilization of integrated geophysical surveying for the safety assessment of levee systems: 24th EEGS Symposium on the Application of Geophysics to Engineering and Environmental Problems, 370–378, https://doi.org/10.4133/1.3614117.

Jiang, M., L. Li, and Q. Yang, 2013, Experimental investigation on deformation behavior of TJ-1 lunar soil simulant subjected to principal stress rotation: Advances in Space Research, **52**, no. 1, 136–146, https://doi.org/10.1016/j.asr.2013.02.001.

Johansen, T. A, P. Digranes, M. van Schaack, and I. Lonne, 2003, Seismic mapping and modeling of near-surface sediments in polar areas: Geophysics, **68**, no. 2, 566–573, https://doi.org/10.1190/1.1567226.

DOI:10.1190/leedff.2022.41.issue-10

Johnston, D. H., M. N. Toksöz, and A. Timur, 1979, Attenuation of seismic waves in dry and saturated rocks: II. Mechanisms. Geophysics, **44**, no. 4, 691–711, https://doi.org/10.1190/1.1440970.

Karunatillake, S., A. Bramson, K. Zacny, C. Dundas, L. Ojha, O. Aharonson, E. Vos, et al., 2021, GANGOTRI mission concept on the glacial key to the Amazonian climate of Mars: Bulletin of the AAS, **53**, no. 4, https://doi.org/10.3847/25c2cfeb.a3d8d8e9.

Knight, R., J. Dvorkin, and A. Nur, 1998, Acoustic signatures of partial saturation: Geophysics, **63**, no. 1, 132–138, https://doi.org/10.1190/1.1444305.

Knopoff, L., 1964, *Q*: Reviews of Geophysics, **2**, no. 4, 625–660, https://doi.org/10.1029/RG002i004p00625.

Kudo, K., and E. Shima, 1970, Attenuation of shear wave in soil: Bulletin of the Earthquake Research Institute. **48**, 145–158.

Li, C., Y. Su, E. Pettinelli, S. Xing, C. Ding, J. Liu, X. Ren, et al., 2020, The moon's farside shallow subsurface structure unveiled by Chang'E-4 Lunar Penetrating Radar: Science Advances, **6**, no. 9, https://doi.org/10.1126/sciadv.aay6898.

Lognonné, P., W. B. Banerdt, W. T. Pike, D. Giardini, U. Christensen, R. F. Garcia, T. Kawamura, et al., 2020, Constraints on the shallow elastic and anelastic structure of Mars from InSight seismic data: Nature Geoscience, **13**, 213–220, https://doi.org/10.1038/s41561-020-0536-y.

Long, L., and A. H. Kocaoglu, 2001, Surface-wave group-velocity tomography for shallow structures: Journal of Environmental and Engineering Geophysics, **6**, no. 2, 71–81, https://doi.org/10.4133/JEEG6.2.71.

Lorenz, R. D., M. Bannister, P. M. Daniell, Z. Krysinski, M. R. Leese, R. J. Miller, G. Newton, P. Rabbetts, D. M. Willett, and J. C. Zarnecki, 1994, An impact penetrometer for a landing spacecraft: Measurement Science and Technology, **5**, no. 9, 1033, https://doi.org/10.1088/0957-0233/5/9/001.

Lorenzo, J. M., D. E. Smolkin, C. White, S. R. Chollett, and T. Sun, 2013, Benchmark hydrogeophysical data from a physical seismic model: Computers and Geosciences, **50**, 44–51, https://doi.org/10.1016/j.cageo.2012.07.034.

Lorenzo, J. M., D. E. Smolkin, C. White, S. R. Chollett, and T. Sun, 2013, Benchmark hydrogeophysical data from a physical seismic model. Data set, https://github.com/cageo/Lorenzo-2012, accessed 13 September 2022.

Lunar Exploration Analysis Group (LEAG), 2016, Lunar human exploration strategic knowledge gap special action team review, https://www.nasa.gov/sites/default/files/atoms/files/leag-gap-review-sat-2016-v2.pdf, accessed 13 September 2022.

Luo, Y., J. Xia, Y. Xu, and C. Zeng, 2011, Analysis of group-velocity dispersion of high-frequency Rayleigh waves for near-surface applications: Journal of Applied Geophysics, **74**, no. 2–3, 157–165, https://doi.org/10.1016/j.jappgeo.2011.04.002.

Mavko, G., T. Mukerji, and J. Dvorkin, 2009, The rock physics handbook: Tools for seismic analysis of porous media (2nd ed.): Cambridge University Press, https://doi.org/10.1017/CBO9780511626753.

Mindlin, R., 1949, Compliance of elastic bodies in contact: Journal of Applied Mechanics, **16**, no. 3, 259–268, https://doi.org/10.1115/1.4009973.

Nakano, Y., and R. Arnold, 1973, Acoustic properties of frozen Ottawa sand: Water Resources Research, **9**, no. 1, 178–184, https://doi.org/10.1029/WR009i001p00178.

National Academies of Sciences Engineering and Medicine (NASEM), 2022, Origins, worlds, and life: A decadal strategy for planetary science and astrobiology 2023–2032: The National Academies Press, https://doi.org/10.17226/26522.

Park, C., 2013, MASW for geotechnical site investigation: The Leading Edge, **32**, no. 6, 656–662, https://doi.org/10.1190/tle32060656.1.

Park, C. B., R. D. Miller, and J. Xia, 1999, Multichannel analysis of surface waves: Geophysics, **64**, no. 3, 800–808, https://doi.org/10.1190/1.1444590.

Park, J.-H., and J.-S. Lee, 2014, Characteristics of elastic waves in sand–silt mixtures due to freezing: Cold Regions Science and Technology, **99**, 1–11, https://doi.org/10.1016/j.coldregions.2013.11.002.

Perko, H. A., J. D. Nelson, and J. R. Green, 2006, Mars soil mechanical properties and suitability of Mars soil simulants: Journal of Aerospace Engineering **19**, no. 3, 169–176, https://doi.org/10.1061/(asce)0893-1321(2006)19:3(169).

Rivera-Valentín, E. G., V. F. Chevrier, A. Soto, and G. Martínez, 2020, Distribution and habitability of (meta)stable brines on present-day Mars: Nature Astronomy, **4**, 756–761, https://doi.org/10.1038/s41550-020-1080-9.

Russell, B., 2019, Machine learning and geophysical inversion — A numerical study: The Leading Edge, **38**, no. 7, 512–519, https://doi.org/10.1190/tle38070512.1.

Shen, J., and J. M. Lorenzo, 2016, Seismic velocity inversion for patchy and homogeneous fluid-distribution conditions in shallow, unconsolidated sands: Geophysics, **81**, no. 5, U51–U60, https://doi.org/10.1190/geo2015-0438.1.

Siegler, M. A., S. E Smrekar, S. Piqueux, N. Müller, and M. Grott, 2014, Three-dimensional thermal modeling for the 2016 InSight mission: Presented at the Eighth International Conference on Mars.

Singhroha, S., S. Bünz, A. Plaza-Faverola, and S. Chand, 2016, Gas hydrate and free gas detection using seismic quality factor estimates from high-resolution P-cable 3D seismic data: Interpretation, **4**, no. 1, SA39–SA54, https://doi.org/10.1190/INT-2015-0023.1.

Slyuta, E. N., 2014, Physical and mechanical properties of the lunar soil (a review): Solar System Research, **48**, 330–353, https://doi.org/10.1134/S0038094614050050.

Sollberger, D., C. Schmelzbach, J. O. Robertsson, S. A. Greenhalgh, Y. Nakamura, and A. Khan, 2016, The shallow elastic structure of the lunar crust: New insights from seismic wavefield gradient analysis: Geophysical Research Letters, **43**, no. 19, 10,078–10,087, https://doi.org/10.1002/2016GL070883.

Spohn, T., T. L. Hudson, E. Marteau, M. Golombek, M. Grott, T. Wippermann, K. S. Ali, et al., 2021, The InSight HP^3 Penetrator (Mole) on Mars: Soil properties derived from the penetration attempts and related activities, https://doi.org/10.48550/arXiv.2112.04438.

Stockwell, J. W., 1999, The CWP/SU: Seismic Unix package: Computers and Geosciences, **25**, no. 4, 415–419, https://doi.org/10.1016/S0098-3004(98)00145-9.

Stokoe, K. H., S. Wright, J. Bay, and J. Roesset, 1994, Characterization of geotechnical sites by SASW method, *in* R. Woods, ed., Geophysical characterization of sites: A. A. Balkema Publishers, 15–25.

Vos, E., O. Aharonson, and N. Schorghofer, 2019, Dynamic and isotopic evolution of ice reservoirs on Mars: Icarus, **324**, 1–7, https://doi.org/10.1016/j.icarus.2019.01.018.

Wathelet, M., 2008. An improved neighborhood algorithm: Parameter conditions and dynamic scaling: Geophysical Research Letters, **35**, no. 9, L09301, https://doi.org/10.1029/2008GL033256.

Xia, J., R. D. Miller, and C. B. Park, 1999, Estimation of near-surface shear-wave velocity by inversion of Rayleigh waves: Geophysics, **64**, no. 3, 691–700, https://doi.org/10.1190/1.1444578.

Xia, J., R. D. Miller, C. B. Park, J. A. Hunter, J. B. Harris, and J. Ivanov, 2002, Comparing shear-wave velocity profiles inverted from multichannel surface wave with borehole measurements: Soil Dynamics and Earthquake Engineering, **22**, no. 3, 181–190, https://doi.org/10.1016/s0267-7261(02)00008-8.

Xiao, L., and J. W. Head, 2020, Geological characteristics of the moon, *in* P. Read et al., eds., Oxford research encyclopedia of planetary science: Oxford University Press, https://doi.org/10.1093/acrefore/9780190647926.013.90

Xu, T.-B., E. J. Siochi, L. Zuo, X. Jiang, and J. H. Kan, 2015, Multistage force amplification of piezoelectric stacks: U.S. Patent 9,048,759 B2.

Yilmaz, O., 2001, Seismic data processing: SEG.